

# Monolithic Germanium/Silicon Photodetectors With Decoupled Structures: Resonant APDs and UTC Photodiodes

Daoxin Dai, *Member, IEEE*, Molly Piels, and John E. Bowers, *Fellow, IEEE*

(Invited paper)

**Abstract**—The Ge/Si system is useful to realize avalanche photodetectors (APDs) operating at 1310–1550 nm because of the intrinsic advantages of complementary metal–oxide–semiconductor (CMOS) compatibility, high light-absorption of Ge, low ionization rate ratio of silicon, and high thermal conductivities of Si and Ge. With the Ge/Si system, it is convenient to realize photodetectors with decoupled structures including resonant Ge/Si APDs as well as uni-traveling carrier (UTC) photodiodes. The resonant Ge/Si APD with a separated absorption-charge-multiplication (SACM) structure, which decouples the light absorption and avalanche process, has high speed, high gain, and high gain-bandwidth product. The UTC photodiode, which decouples the light absorption and the carrier collection, is useful for high-power applications. This paper first reviews the structure and model of decoupled Ge/Si (A)PDs, particularly, the equivalent circuit models for explaining the peak enhancement of the frequency response in resonant SACM APDs. This model is also applied to UTC Ge/Si PDs developed recently for the high-power applications.

**Index Terms**—Avalanche, photodetector, peak enhancement, uni-traveling carrier (UTC), Si, Ge.

## I. INTRODUCTION

As it is well known, silicon photonics is very promising and has attracted extensive attention for cost-effective and high-performance optical interconnects (particularly, photonic network-on-chip) [1]. Many silicon photonic integrated devices have been demonstrated successfully, particularly, ultra-compact passive devices. However, the intrinsic properties of silicon make it challenging to realize active photonic integrated devices, like lasers and modulators, as well as photodetectors. A general solution for this issue is developing a hybrid-integration platform combining another appropriate active material on silicon. For example, hybrid silicon lasers have been developed successfully by bonding [2] or epitaxially growing a III–V layer on silicon [3]. For photodetectors, since silicon is transparent in the

wavelength range of 1.3–1.55  $\mu\text{m}$  used for optical fiber communications, a material with a smaller bandgap is needed to achieve an efficient light absorption for generating photo-carriers [4]–[7]. Among various small-bandgap materials, germanium is one of the most attractive candidates because of the strong linear absorption up to 1.55  $\mu\text{m}$ , as well as CMOS compatibility. The measured absorption coefficient is about  $10\,000\text{ cm}^{-1}$  at 1.31  $\mu\text{m}$  and  $5,000\text{ cm}^{-1}$  at 1.55  $\mu\text{m}$  [8]. The Ge absorption range can be extended up to 1.6  $\mu\text{m}$  by utilizing bandgap shrinkage related to tensile strain [9], [10].

Note that there is a large lattice mismatch between Ge and Si ( $\sim 4.2\%$ ), which results in a high concentration of dislocations and makes it difficult to realize the epitaxial growth of high-quality thick germanium layers on silicon. Fortunately, great progress has been made on the growth of germanium on silicon in recent years [10]–[13]. Many approaches have been demonstrated. One approach to minimize the misfit dislocation density is with a two-step Ge epitaxial deposition [9], [14]: 1) a thin Ge buffer layer (30–50 nm) is grown at low temperature (400  $^{\circ}\text{C}$ ) to localize misfit dislocations while still keeping a smooth surface; 2) a thick Ge film growth at higher temperature (730  $^{\circ}\text{C}$ ) [14]. Continuous or cyclic thermal treatment has also been demonstrated as an effective way to further reduce defect density inside Ge epilayers [15], [16]. The threading dislocation density can be significantly reduced to  $\sim 5 \times 10^6/\text{cm}^2$  [4], as compared to the pre-annealing concentration ( $>10^8/\text{cm}^2$ ). With the techniques of high-quality Ge growth on silicon, many Ge-on-Si photodetectors have been demonstrated, including metal–semiconductor–metal (MSM) [17] and PIN devices [18].

In general, there are two ways of illuminating a photodetector [19], [20]. One is surface illumination to realize normal-incidence photodetectors for free-space or fiber-optic coupling [4], and the other is edge coupling to realize waveguide-type photodetectors for on-chip integration [21], [22]. It is well known that there is a trade-off between quantum efficiency, bandwidth, and dark current for normal-incidence photodetectors [19]. This can be overcome in a waveguide-type Ge/Si photodetector because the carrier collection is implemented in a direction perpendicular to the light propagation (absorption) direction [6]. In this way, the light absorption length is *decoupled* from the carrier collection path, and consequently, one can realize high-speed waveguide-type photodetectors with almost 100% quantum efficiency.

Manuscript received January 31, 2014; revised April 6, 2014; accepted March 20, 2014. This work was supported by the Defense Advanced Research Projects Agency.

D. Dai is with the Centre for Optical and Electromagnetic Research, State Key Laboratory for Modern Optical Instrumentation, Zhejiang University, Hangzhou 310058 China (e-mail: dxdai@zju.edu.cn).

M. Piels and J. E. Bowers are with the Department of Electrical and Computer Engineering, University of California Santa Barbara (UCSB), Santa Barbara, CA 93106 USA (e-mail: mopi@fotonik.dtu.dk; bowers@ece.ucsb.edu).

Color version of one or more of the figures in this paper are available online at <http://ieeexplore.ieee.org>.

Digital Object Identifier 10.1109/JSTQE.2014.2322443

As mentioned earlier, Ge has efficient light absorption in the wavelength range of 1.3–1.55  $\mu\text{m}$ . Meanwhile, silicon has a low  $k < 0.1$  (defined as the ratio of the ionization rate of one carrier type to the other), which makes it an ideal multiplication material [23]. Therefore, the Ge-on-Si platform is very attractive for realizing avalanche photodiodes (APDs). Compared to receivers with p-i-n photodiodes, APDs achieve 5–10 dB better sensitivity due to their internal multiplication gain, and they have been utilized for a wide range of commercial, military, and research applications [24]. The operation principle of an APD is based on photo-carrier generation in the absorption layer and the impact ionization process for carrier multiplication. It is well known that a separated absorption-charge-multiplication (SACM) structure is one of the most attractive designs for APDs because the thickness of the multiplication region is decoupled from the charge density constraint in separate-absorption-multiplication APDs. The SACM structure and low  $k$ -value of silicon lead to low excess noise and high gain-bandwidth product (GBP) APDs [4]. In silicon, the multiplication process is dominated by electrons. Hawkins *et al.* reported bonded InGaAs/Si SACM APDs with GBP of 320 GHz. The first CMOS-compatible Ge/Si SACM APD was demonstrated by Kang *et al.* with a GBP as high as 340 GHz [4]. Later Duan *et al.* also demonstrated a Ge/Si SACM APDs with a GBP of  $\sim 310$  GHz [5]. Currently, Ge/Si APDs have been very competitive in high-speed optical communication systems with higher GBPs and better sensitivity compared to traditional group III-V APDs [6]. Recently, Ge/Si APDs have been applied to other fields, such as single-photon detection [25].

In addition, the Ge/Si system is an appealing candidate to realize high-efficiency fast photodiodes with large saturated output power for high-power applications, such as microwave photonics, because of the high thermal conductivities of Si and Ge, the durability, and low cost of the substrate material [26]–[29]. In order to have good efficiency as well as large bandwidth, a uni-traveling carrier (UTC) design is usually used in photodiodes to *decouple* the photo-carrier generation region and the depletion region. Similar to the case with APDs, this decoupling of absorption and depletion region thickness allows for independent optimization of efficiency, bandwidth, and power-handling. In recent years, Ge/Si UTC photodiodes have been realized with high performance [30], [31].

In this paper, recent progress on Ge/Si APDs and UTC photodiodes is reviewed. First, we focus on the peak enhancement of the frequency response observed in Ge/Si APDs, which is a key to achieve an ultra-high GBP (840 GHz) [32]. The origin of the peak enhancement in Ge/Si APDs is discussed through small signal models. Second, high-power Ge/Si UTC photodiodes are discussed, including their design and characterization.

## II. RESONANT Ge/Si APDS

### A. Structure of Ge/Si APDs

Ge/Si photodiodes are usually based on MSM [17] or PIN diode structures [18]. For the PIN type, there is an intrinsic Ge layer for the absorption region and a p-type heavily doped silicon layer at the bottom as the p-electrode [see Fig. 1(a)] [33]–[36].

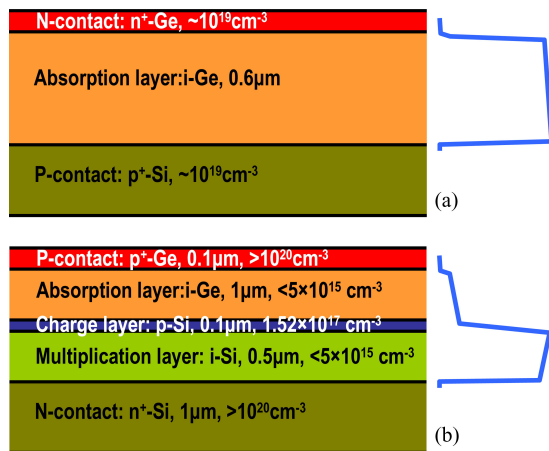


Fig. 1. Cross section of a Ge/Si PD (a), and a Ge/Si APD (b).

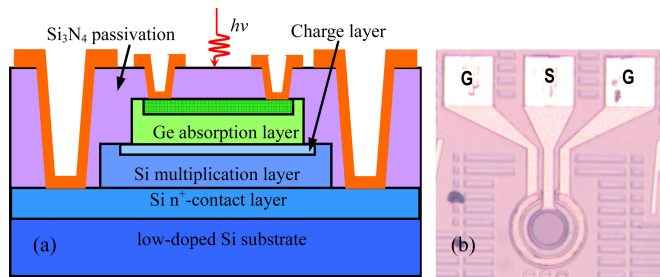


Fig. 2. (a) Schematic configuration of the Ge/Si SACM APD; (b) Microscope picture for the top view of a Ge/Si SACM APD.

When a reverse bias is applied to the PIN diode, there is a nearly uniform electric field in the intrinsic Ge region, as shown in Fig. 1(a). The thickness of the intrinsic Ge layer should be optimized to maximize the 3 dB bandwidth by considering the transit time constant as well as the resistance–capacitance ( $RC$ ) time constant of the PIN diode. The highest bandwidth reported to date for free-space coupled Ge/Si p-i-n photodiodes is 49 GHz at  $-2$  V reverse bias [37].

A Ge/Si APD has a more complicated layer structure than a Ge/Si photodiode. Fig. 1(b) shows the schematic configuration of an SACM Ge/Si APD [4], which consists of a Ge absorption layer, a Si charge layer, and a Si multiplication layer. The charge layer is usually thin ( $\sim 0.1$   $\mu\text{m}$ ) and the doping is moderate, e.g.,  $1.5 \times 10^{17}\text{cm}^{-3}$ , which is optimized to achieve an appropriately high electric field in the Si multiplication layer to generate impact ionization processes. Meanwhile, the electric field in the Ge absorption layer should be low enough to avoid undesired multiplication in Ge.

For Ge/Si APDs, there are usually two methods of illumination: the *normal-incidence* type, which is usually used for free-space or fiber-coupling applications, as well as the *waveguide-type*, which is preferred for on-chip integration.

1). *Normal-Incidence Ge/Si APDs* [4]: Fig. 2(a) shows the cross section of a normal-incidence SACM Ge/Si APD, which has the layer structure given in Fig. 1(b). With the SACM design, one can optimize the thicknesses for the Ge absorption

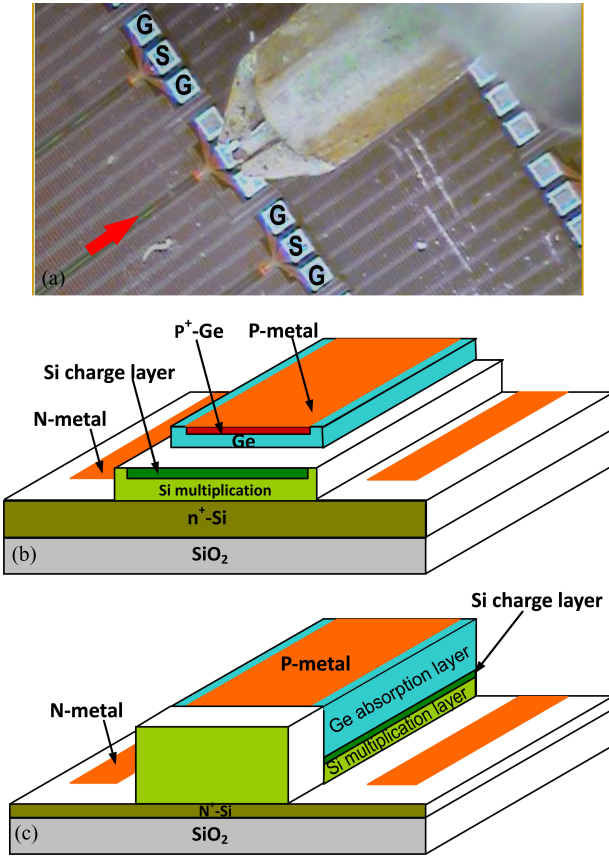


Fig. 3. (a) Microscope picture for the top view of a waveguide-type Ge/Si SACM APD; (b) Schematic configuration of an evanescently-coupled waveguide-type Ge/Si APD; (c) Schematic configuration of a butt-coupled waveguide-type Ge/Si APD.

layer and the Si multiplication layer separately to improve the quantum efficiency and the multiplication gain. A silicon-nitride film is deposited on the top surface of the photodiode to serve as an anti-reflection coating for further improvement of the quantum efficiency. When light enters the Ge absorption region, photo-carriers are generated and the electrons drift to the Si multiplication region due to the electric field. The photo-generated electrons undergo a series of impact ionization processes in the silicon multiplication region due to the high electric field there. As a result, the photocurrent is amplified and the sensitivity is improved.

2). *Waveguide-Type Ge/Si APDs.* [38]: Fig. 3(a) shows waveguide-type Ge/Si APDs, which have been developed rapidly in recent years because they decouple the light absorption length from the carrier collection path so that one can obtain a high-speed and a high-responsivity photodetector, simultaneously. For waveguide-type Ge/Si APDs, which are useful for on-chip integration, there are two popular methods of coupling [18], [39]: evanescent coupling and butt-coupling, as shown in Fig. 3(b) and (c), respectively. For the evanescently coupled case, light guided in the silicon optical waveguide will be coupled evanescently to the germanium layer and be absorbed [38]. The thickness of the Ge absorption layer should be optimized to maximize the evanescent coupling efficiency so that the

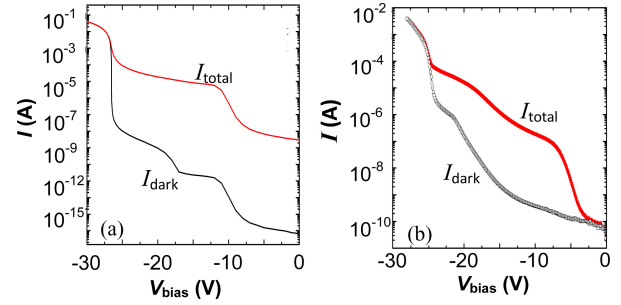


Fig. 4.  $I$ - $V$  curves for Ge/Si APDs, (a) calculated; (b) measured. [32].

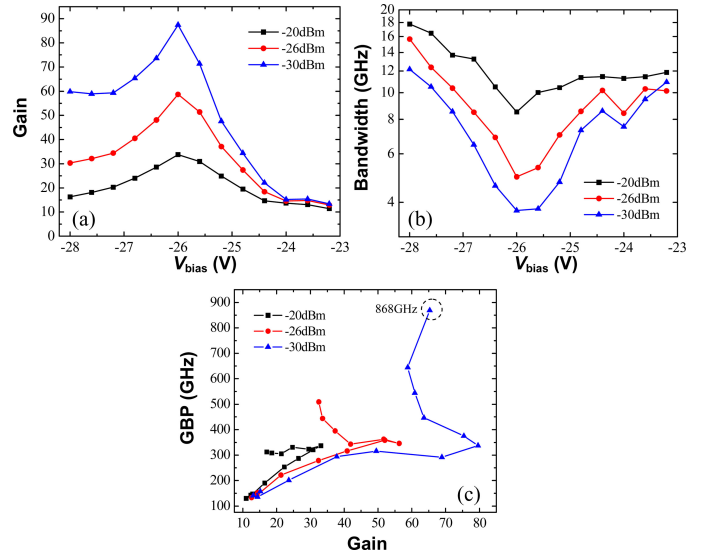


Fig. 5. (a) The measured gain, (b) bandwidth, and (c) GBP versus the bias voltage for a normal-incidence SACM Ge/Si APD under  $P_{\text{in}} = -20$  dBm,  $-26$  dBm, and  $-30$  dBm at  $\lambda = 1310$  nm [32].

photodetector length can be minimized, which is helpful to reduce the junction capacitance as well as the dark current [31]. On the other hand, it is evident that butt-coupling is more efficient than evanescent coupling because light directly enters the Ge absorption layer, which helps shorten the photodiode length to achieve higher bandwidth without compromising the responsivity [40]. However, the fabrication of the butt-coupled APD is complicated.

### B. Gain and Bandwidth of Ge/Si APDs

Fig. 4(a) and (b) shows the calculated and measured total currents of a normal-incidence SACM Ge/Si APD (as an example) for the dark case and the case with an optical illumination of  $P = -20$  dBm, respectively. From Fig. 4(a), one sees the break through voltage is around  $-26.4$  V, which agrees with the measured value [see Fig. 4(b)]. Fig. 5(a) shows the measured gain of a normal-incidence Ge/Si APD with a diameter  $D = 30$   $\mu\text{m}$  at different optical powers as the bias is varied [32]. The gain is determined by normalizing the APD responsivity to the primary responsivity ( $\sim 0.55$  A/W at 1310 nm) of a p-i-n device fabricated on the same wafer. From Fig. 5(a), it can be

seen that there is a maximum of the gain around  $V_{\text{bias}} = -26$  V, which is similar to those results reported for APDs based on other material systems [41]–[43]. Fig. 5(a) also shows that the gain becomes lower when the optical power is increased. The significant dependence of the gain on the optical input power is because the electric field in the multiplication region is redistributed due to the large amount of photo-carriers generated [32].

Fig. 5(b) shows the measured 3 dB-bandwidth of the normal-incidence Ge/Si APD. It can be seen that the 3 dB-bandwidth is also strongly dependent on the bias voltage. The 3 dB-bandwidth decreases as the bias varies from  $-23$  to  $-26$  V and an enhancement is observed when increasing the bias further to  $-26$ – $-28$  V. This 3 dB-bandwidth enhancement helps obtain an ultrahigh GBP, as given in Fig. 5(c), which shows the extracted GBP of the APD with different input powers. It can be seen that the highest GBP measured is 868 GHz at  $P_{\text{in}} = -30$  dBm, corresponding to a gain of 65.3 and a bandwidth of 13.3 GHz. When the gain is low (at low bias), the APD works like a PIN-photodiode whose 3 dB-bandwidth is almost constant, and consequently, the APD's GBP increases proportionally to the gain. As the gain increases, the bandwidth drops due to the multiplication build-up time, and thus, the GBP becomes saturated ( $\sim 300$  GHz), which is similar to those reported [4]. However, beyond the gain peak, the GBP starts to increase again dramatically because of the 3 dB-bandwidth enhancement observed in Fig. 5(b). This 3 dB-bandwidth enhancement is due to a strong enhancement of response in the high frequency range, which can be seen clearly from the measured frequency responses given in Fig. 6(a) [44]. Such an enhancement is also observed for APDs with larger diameters ( $D = 50$ , 80, and  $150 \mu\text{m}$ ) when the reverse bias is high enough, as shown in Fig. 6(b)–(d). For example, the maximum peak enhancement for the APD with  $D = 80 \mu\text{m}$  is as large as 4 dB when it operates at  $V_{\text{bias}} = -26.6$  V.

Fig. 6(e) shows the extracted 3 dB-bandwidth for the Ge/Si APDs with different diameters  $D$ . It can be seen that the bandwidths at low voltages for the cases of  $D = 30$ , 50, 80, and  $150 \mu\text{m}$  are about 10.4, 7.1, 4.4, and 1.3 GHz, respectively. This bandwidth is inversely proportional to the area of the APD as expected since it is mainly limited by the  $RC$  constant. At high voltages, the bandwidth increases significantly due to the peak enhancement. For example, for the case of  $D = 50 \mu\text{m}$ , the bandwidth is as high as 16 GHz at  $V = -27.6$  V. Similar phenomena have also been reported for waveguide-type Ge/Si APDs [38], Si-SiGe-based APDs (at 830 nm) [42], Si APDs [43], and InGaAs/InAlAs APDs [45].

In order to understand the peak enhancement shown in Fig. 6(a)–(d), one can examine the APD impedance by measuring the microwave reflection parameter  $S_{22}$  as the bias voltage varies. In Fig. 7(a)–(c), the measured results for  $D = 150$ , 80, and  $50 \mu\text{m}$  are shown for the frequency range from 45 MHz to 30 GHz, respectively. It can be seen that the measured  $S_{22}$  for all three devices changes similarly. For example, for the APD with  $D = 80 \mu\text{m}$ , the entire curve is below the line  $\Gamma_i = 0$  when the bias voltage is low (e.g.,  $V = -24.6$  V). This is very similar to the behavior of a PIN photodiode (whose equivalent circuit consists

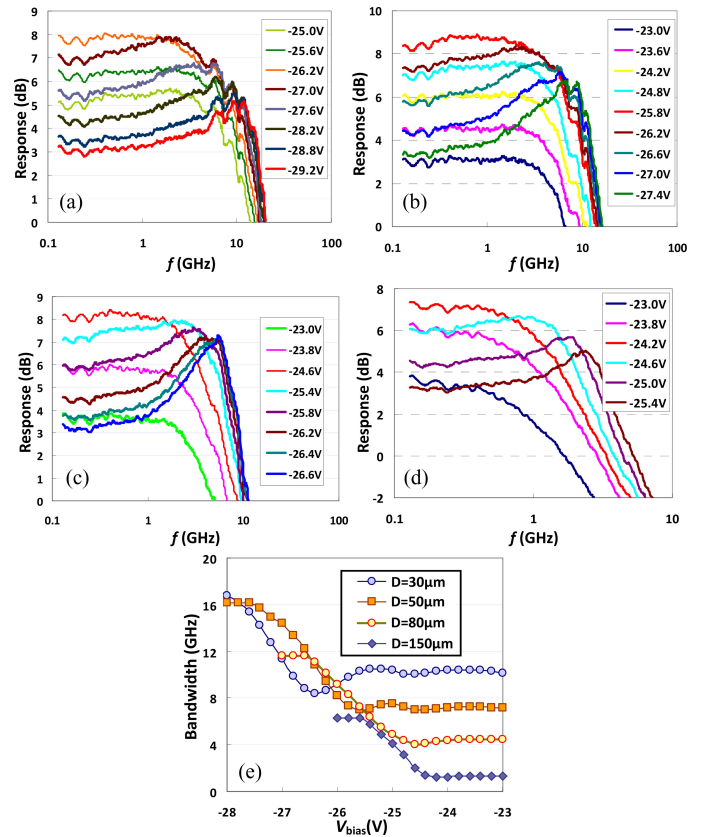


Fig. 6. Measured frequency responses at different bias voltages for normal-incidence SACM Ge/Si APDs with diameters (a)  $D = 30 \mu\text{m}$ , (b)  $D = 50 \mu\text{m}$ , (c)  $D = 80 \mu\text{m}$ , and (d)  $D = 150 \mu\text{m}$ ; (e) The bandwidths for the SACM Ge/Si APDs with different diameters.

of a resistor and capacitor in parallel, representing the diode capacitance and diode resistance), as expected. When operating at a higher bias voltage, the parameter  $\Gamma_i$  becomes positive in the frequency range from 0 to a certain value  $f_0$ . This phenomenon becomes stronger when the bias voltage increases further.

Fig. 8(a) and (b), respectively, shows the real part  $Z_r$  and the imaginary part  $Z_i$  of the measured impedance  $Z$  for the APD with  $D = 80 \mu\text{m}$ . At relatively high voltage (e.g.,  $V > 25.4$  V), the real part  $Z_r$  has a peak at a certain frequency  $f_r$ , while the imaginary part  $Z_i$  has a transition from a positive value to a negative value around  $f_r$ . This is similar to the impedance of an  $LC$  resonator. Therefore, this kind of APD is called a “resonant APD” whose equivalent circuit might have an  $LC$ -resonator [44]. In order to explain the origin of the peak enhancement (resonance), modeling with small-signal analysis has been presented and the corresponding equivalent circuit including  $LC$ -elements has been derived [46], [47], which will be reviewed in the following section.

### C. Modeling and Equivalent Circuits for Ge/Si APDs

Since the electric field distribution in an SACM Ge/Si APD is similar to that in an impact ionization avalanche transit-time (IMPATT) diode structure, one can make an analysis similar to that shown in Ref. [48]. In the avalanche region, the impact

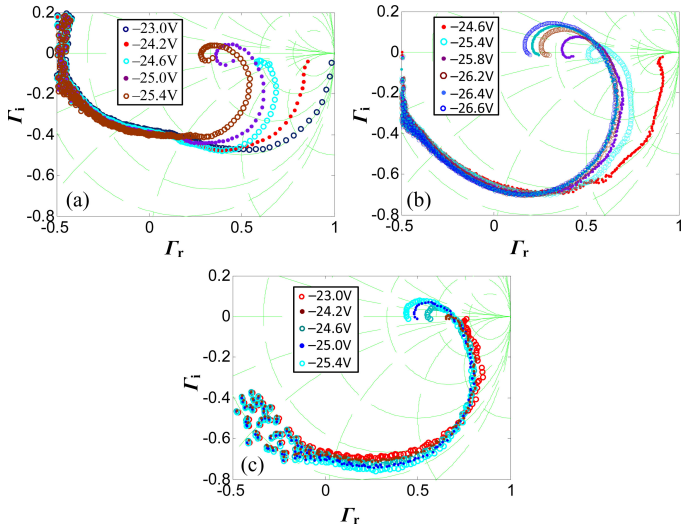


Fig. 7. Measured  $S_{22}$  at different bias voltages for SACM Ge/Si APDs with (a)  $D = 150 \mu\text{m}$ , (b)  $D = 80 \mu\text{m}$ , and (c)  $D = 50 \mu\text{m}$ . [44].

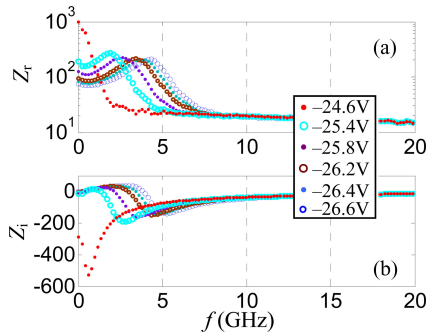


Fig. 8. Measured impedance  $Z$  at different bias voltages for an SACM Ge/Si APD with  $D = 80 \mu\text{m}$ : (a) the real part  $Z_r$ ; (b) the imaginary part  $Z_i$ . [44].

ionization process introduces a delay between the ac current and the electric field (i.e., the ac voltage), which is equivalent to an inductance [44], [46]. This has been verified recently for APDs by simulation with a self-consistent Monte Carlo simulation tool based on physics-level description of carrier transport [49]. Therefore, an equivalent circuit model with an  $LC$ -circuit for the avalanche region can be applied to Ge/Si APDs [44].

In Ref. [46], the impedance of the Ge/Si APD as well as the corresponding equivalent circuit with an inductance is derived according to a small-signal model based on the Poisson Equation and the semiconductor transport equations. The small-signal model is also useful for calculating the frequency response of APDs directly [46]. For this model, the electric field (and hence the ionization rate) is assumed to be uniform in the avalanche region for simplicity [50], [51]. For an APD with an arbitrary layer structure and absorption/ionization coefficients, in Ref. [47], a simple matrix method is presented and the impedance as well as the equivalent circuit are derived.

In following section, we give a review of the model and analysis for the impedance of the Ge/Si APD as well as the corresponding equivalent circuit to explain the origin of the peak

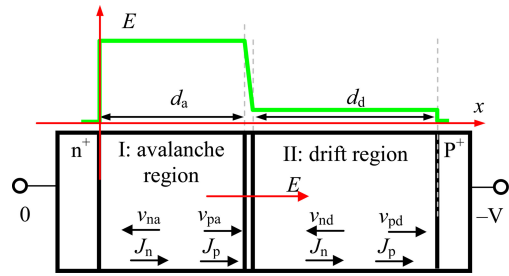


Fig. 9. Structure and electric field distribution for an SACM APD.

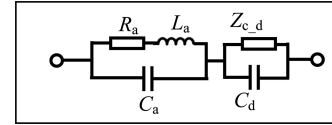


Fig. 10. Simplified equivalent circuit for the APD impedance  $Z$ .

enhancement of frequency response observed. Here, normal-incidence SACM Ge/Si APDs are considered as an example, while the equivalent circuit is also applicable to waveguide-type SACM Ge/Si APDs [38].

1). *Small-Signal Model and Analysis*: Fig. 9 shows the configuration of a generic SACM APD. Here, the drift region is the light absorption region. There is thin charge layer between the avalanche layer and the drift layer. The doping level of the charge layer is optimized to achieve sufficient high electric field in the avalanche region (see Fig. 9). Since the charge layer is usually very thin (100 nm in Ref. [4]), the APD structure is simplified to include an avalanche layer and an absorption layer only, with uniform electric fields in each [46]. Finally, the avalanche region and the drift region can be modeled separately.

A similar small-signal model has been developed for IMPATT oscillators, usually with the assumption that the electrons and the holes have equal ionization rates and velocities [50]. In [51], Manasse *et al.* considered the differences in hole and electron velocities and ionization rates and gave an improved dispersion relationship of a P-N junction avalanche diode, however, for the case with a *single* uniform depletion layer.

In Ref. [46], a general case that the electrons and the holes have different ionization coefficients and different velocities is considered, and a small-signal model is obtained from the basic equations for carrier transport in the avalanche region, as well as in the drift region. The model is able to calculate the impedance characteristic and the frequency response of an SACM APD that has different parameters for the absorption layer and the multiplication layer.

With the small-signal model, a simplified equivalent circuit for the APD impedance is also derived as shown in Fig. 10 [46]. This equivalent circuit for the avalanche region includes an inductance  $L_a$ , a resistance  $R_a$ , and a capacitance  $C_a$ . The expressions ( $L_a$ ,  $R_a$ , and  $C_a$ ) for these elements are given in [46]. It shows that the inductance  $L_a$  and the series resistance  $R_a$  are inversely proportional to the direct current  $\bar{J}S$  ( $S$  is the APD area) and the derivative  $\alpha' = d\alpha/dE$  ( $\alpha$  is the ionization

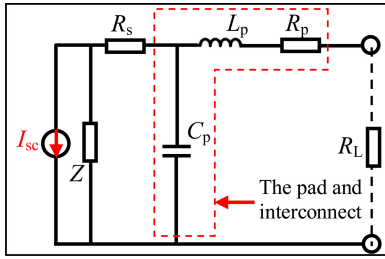


Fig. 11. APD equivalent circuit including parasitic effects.

rate of electrons). The inductance  $L_a$  and the series resistance  $R_a$  are explained as follows. When an ac voltage is applied to the avalanche region, both the ionization coefficient and the carrier density are modulated. The time variation of the electron density  $\partial n/\partial t$  (as well as  $\partial p/\partial t$ ) is not only related to the ac electric field but also the carrier density itself. The interaction between the ac electric field and the ac carrier density introduces an inductance with a series resistance. Particularly, the inductance is due to the phase delay between the ac-current and the electric field (i.e., the ac voltage). In the drift region, there is no avalanche process, and consequently, no inductance effect. The impedance  $Z_{cd}$  is the part corresponding to the conduction current. Usually the inductance ranges from sub-nH to several nH and the series resistance  $R_a$  ranges from hundreds of Ohm to several Ohm, which depends on the value to the direct current  $\bar{J}S$  and the derivative  $\alpha'$ .

This simplified equivalent circuit is helpful for understanding the behavior of the APD impedance and frequency response. In order to achieve greater accuracy, one can also directly use the impedance  $Z$  of an SACM APD in the equivalent circuit including the parasitic effects of series resistance ( $R_p$ ), transmission line inductance ( $L_p$ ), and pad capacitance ( $C_p$ ), as shown in Fig. 11. From this figure, the current flowing through the load resistance  $R_L$  is given by  $I_L = I_{sc}\kappa$ , where the coefficient  $\kappa$  can be obtained easily according to the equivalent circuit in Fig. 11.

The real part  $Z_r$  and the imaginary part  $Z_i$  of the calculated impedance  $Z$  are shown in Fig. 12(a). When the electric field is relatively weak (e.g.,  $E = 385$  kV/cm), the real part  $Z_r$  is positive and decreases monotonically with frequency, while the imaginary part  $Z_i$  is negative and has a minimal value at a certain frequency. This behavior is essentially like a PIN detector, which is equivalent to a parallel connected  $RC$  circuit. When the electric field is stronger, the impedance  $Z$  becomes very different [see the curves of  $E > 400$  kV/cm in Fig. 12(a)]. The real part  $Z_r$  of the impedance  $Z$  has a peak at a certain frequency  $f_r$  and the imaginary part  $Z_i$  of the impedance has a transition from a positive to a negative value at almost the same position  $f_r$ . This indicates that there is a  $LC$  resonator in the equivalent circuit. When  $f < f_r$ , the imaginary part  $Z_i$  is positive since the inductance plays a dominant role. When  $f > f_r$ , the capacitance plays a dominant role, and consequently, the imaginary part  $Z_i$  becomes negative. Fig. 12(b) and (c) shows the calculated impedance with the parasitic effects of the probe pads, and the measured impedance for the APD with  $D = 80$   $\mu\text{m}$ , respectively. For the calculation, the elements representing the

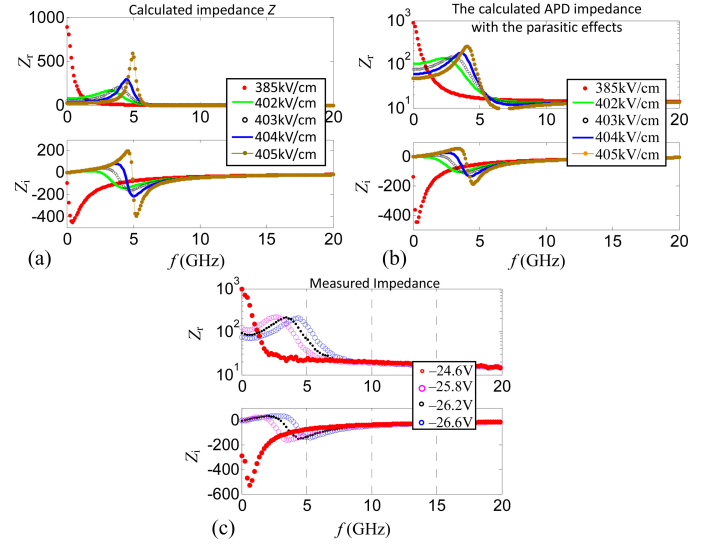


Fig. 12. The real part and the imaginary part of the impedance for: (a) the APD without parasitic effects; (b) the APD with parasitic effects ( $R_p$ ,  $C_p$ , and  $L_p$ ); (c) the measured impedance of the APD. [46].

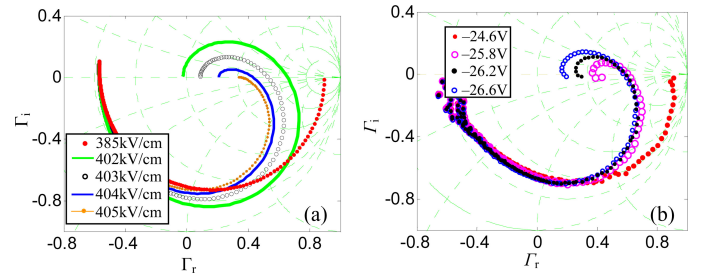


Fig. 13. (a) Calculated microwave reflection coefficient plotted on the Smith chart (the frequency ranges from 45MHz to 30GHz); (b) Measured reflection coefficient.

parasitic effects are  $L_p = 82$  pH,  $C_p = 0.193$  pF, and  $R_p = 6.65$   $\Omega$ , which are estimated from the experimental measurements. It can be seen that the calculated results are very close to the measurement results. The calculated and the measured Smith charts given in Fig. 13(a) and (b) also show excellent agreement.

On basis of the equivalent circuit given in Fig. 11, the frequency responses of the Ge/Si APDs under operation with different electric field strength can be easily calculated, as shown in Fig. 14(a). As the electric field strength increases, the dc gain increases because of more impact ionization [as can be seen in the responses in the low-frequency range shown in Fig. 14(a)]. As the electric field strength in the multiplication region increases (e.g.,  $E > 402$  KV/cm here), the response at low frequency decreases, while there is a peak enhancement in the high frequency range, which is very similar to the measured results [see Fig. 14(b)].

The origin of the peak enhancement can be seen more clearly from Fig. 14(c), which shows the calculated frequency response for the case  $E = 405$  kV/cm as an example. In Fig. 14(c), the top curve is for the short-circuit frequency response of

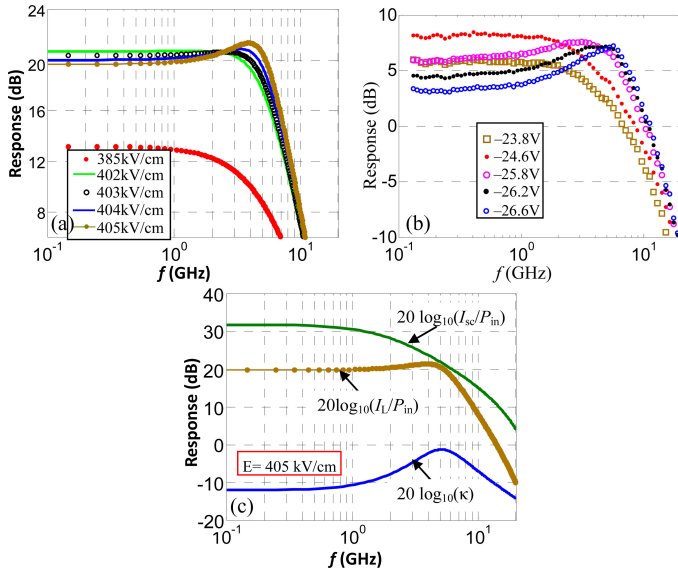


Fig. 14. (a) Calculated frequency responses at different electric field strengths; (b) Measured frequency responses at different bias voltages; (c) the response when  $E = 405$  kV/cm. [46].

APD, which is given by  $20\log_{10}(I_{sc}/P_{in})$ . The bottom curve is the response for  $\kappa$ , which is given by Eq. (19) in Ref. [46], and consequently, the parasitic effects are included. The dotted curve is the frequency response of the current flowing through the load resistance, which is given by  $20\log_{10}(I_L/P_{in}) = 20\log_{10}(\kappa; I_{sc}/P_{in})$ . From this figure, one sees the peak-enhancement of the response  $20\log_{10}(I_L/P_{in})$  corresponds to the peak of the coefficient  $\kappa$ . Furthermore, the peak of the coefficient  $\kappa$  coincides with the maximal value of the impedance  $Z$  without the parasitic effects (see Fig. 12).

2). *A Simple Matrix Method for Small-Signal Analysis:* The reported analytical small-signal modeling was achieved with the following assumptions: 1) the electrons and holes have equal ionization rates and velocities [50]; 2) the electric field (and hence, the ionization rate) is uniform in the avalanche region [50], [51]; 3) the absorption is uniform in the absorber and zero in the drift region [49], [52]. With these assumptions, one could obtain some simple analytical expressions for APDs, and consequently, these models are helpful to achieve some physical explanation of device behavior.

However, these assumptions may not be true for APDs where the ionization rate and the absorption are position-dependent. Therefore, it is desirable to have a simple and complete model. In Ref. [47], small-signal modeling based on a simple matrix method is presented to calculate the impedance characteristic and the frequency response of an APD with an arbitrary layer structure and absorption/ionization coefficients. For this matrix method model, the depletion region of the APD is divided into many thin sub-layers (as shown in Fig. 15). In each sub-layer, the ionization rates ( $\alpha$  and  $\beta$ ) and the carrier-generation rate  $g$  are assumed to be uniform (as shown below) so that analytical expressions for the distributions of the ac current density and the ac electrical field in each sub-layer can be obtained. The matrix

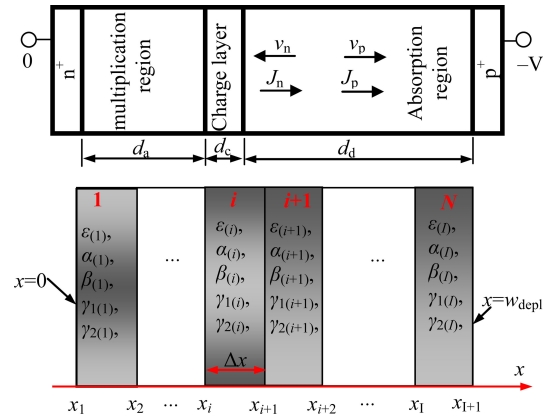


Fig. 15. Schematic structure for an SACM-APD and the sub-layers in the model.

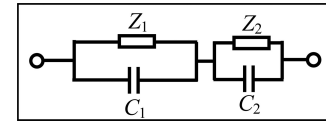


Fig. 16. Equivalent circuit for the depletion region of an SACM Ge/Si APD.

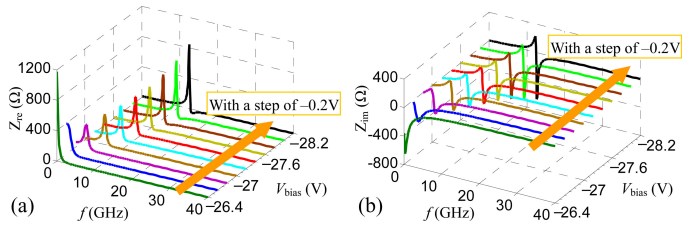


Fig. 17. Calculated impedance  $Z$  for the whole depletion region at various reverse bias voltages  $V_{bias}$  when the optical input power is  $-20$  dBm, (a) the real part  $Z_{re}$ ; (b) the imaginary part  $Z_{im}$ . [47].

formulas for the whole depletion region are then obtained by using the boundary conditions between two adjacent sub-layers [47].

According to the formula and analysis in Ref. [47], the Si layer (including the avalanche region and the charge layer) and the Ge layer (i.e., the absorption region) in a Ge/Si APD is equivalent to a complex impedance ( $Z_1$  or  $Z_2$ ) in parallel with a capacitance ( $C_1$  or  $C_2$ ). Consequently, one has the equivalent circuit for the depletion region of the Ge/Si SACM APD as shown in Fig. 16.

With this matrix method, one can simulate resonant Ge/Si SACM APDs [4]. Fig. 17(a) and (b), respectively, show the real part and the imaginary part of the calculated impedance  $Z$  (see Eq. (12) in Ref. [47]) for the whole depletion region (including the Si region and the Ge region) as an example.

In order to determine the equivalent circuit for the SACM APD, one can calculate the impedances  $Z_2$  and  $Z_1$  for the Ge layer (the absorption region) and the Si layer (i.e., the avalanche region and the charge layer) separately. Usually the impedance and the equivalent circuit for the avalanche region is the focus

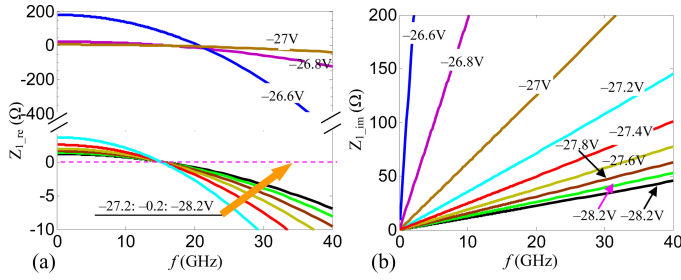


Fig. 18. Calculated impedances  $Z_1$  for the Si layer (including the avalanche, and charge layers) at different reverse bias voltages: (a) the real part  $Z_{1,real}$ ; (b) the imaginary part  $Z_{1,im}$ .

TABLE I  
THE FITTING PARAMETERS OF THE EQUIVALENT CIRCUIT FOR THE SI LAYER  
(INCLUDING THE AVALANCHE REGION AND THE CHARGE LAYER)

$V_{bias}$ (V)	-26.8	-27	-27.2	-27.4	-27.6	-27.8	-28	-28.2
$I_0$ (mA)	3.53	11.77	21.32	31.12	41.01	50.97	60.96	70.98
$R_1$ (Ω)	23	6.6	3.66	2.56	2	1.56	1.36	1.19
$R_0$ (Ω)	-4400	-1450	-835	-580	-430	-365	-305	-265
$L$ (nH)	3.2	1.03	0.59	0.41	0.31	0.255	0.215	0.185

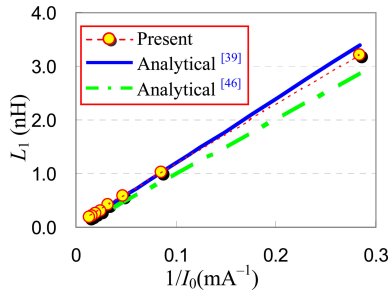


Fig. 19. Fit inductance  $L_1$  in Table I as the current  $I_0$  varies. [47].

because of the resonance (which, contributes to the peak enhancement of the frequency response).

Fig. 18(a) and (b), respectively, show the real part  $Z_{1,real}$  and imaginary part  $Z_{1,im}$  for the calculated impedance  $Z_1$  for the Si layer (including the avalanche region and the charge layer) at various bias voltages (ranging from  $-26.6$  to  $-28.2$  V). Fig. 18(b) shows that the imaginary part  $Z_{1,im}$  increases almost linearly with the frequency, which indicates that the impedance behaves like an inductance (whose impedance is proportional to the frequency). According to Fig. 18(a) and (b), the impedance  $Z_1$  for the avalanche region can be fitted by an equivalent circuit including a negative resistance  $R_0$ , and an inductance  $L_1$  with a series resistance  $R_1$  connected in parallel. The fitting parameters are given in Table I. Particularly, the inductance  $L_1$  (see Table I) is plotted in Fig. 19 as the dc current  $I_0$  varies. It can be seen that there is an almost linear relationship between the inductance  $L_1$  and the reciprocal ( $1/I$ ) of the current. The inductances calculated using the

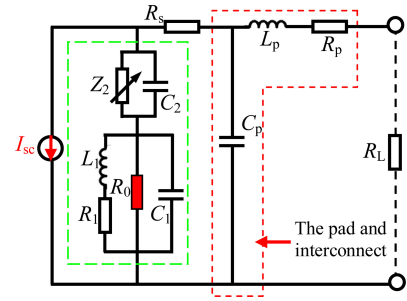


Fig. 20. Equivalent circuit for the whole Ge/Si SACM APD device (including the parasitic elements,  $C_p$ ,  $L_p$  and  $R_p$ ).

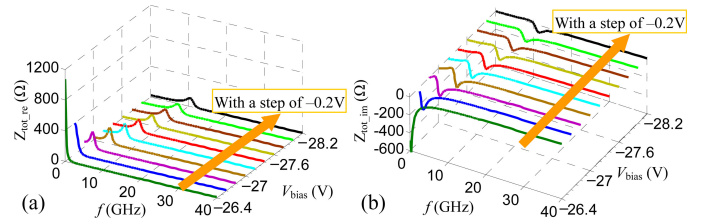


Fig. 21. Calculated total impedance  $Z_{tot}$  of the APD (including the parasitic elements) at various reverse bias voltages when the optical input power is  $-20$  dBm, (a) the real part  $Z_{tot,real}$ ; (b) the imaginary part  $Z_{tot,im}$ . [47].

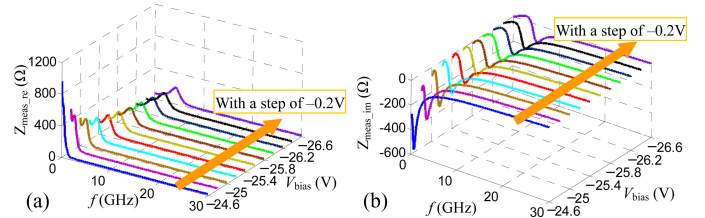


Fig. 22. Measured APD impedance  $Z_{meas}$  (including the parasitic elements) at various bias voltages, (a) the real part  $Z_{meas,real}$ ; (b) the imaginary part  $Z_{meas,im}$ . [47].

following analytical formulas:  $L = (d_a/v_e)/(2\alpha'I_0)$  [49], and  $L = [d_a/(v_e + v_h)]/\alpha'I_0$  [46] are also shown. It can be seen that the formula  $L = [d_a/(v_e + v_h)]/\alpha'I_0$  given in Ref. [46] gives a better estimation for the inductance because the slight difference between the saturation velocities of electrons and holes has been taken into account.

Fig. 20 shows the equivalent circuit for the whole APD including the parasitic elements ( $C_p$ ,  $L_p$ , and  $R_p$ ) [47]. The real part  $Z_{tot,real}$  and the imaginary part  $Z_{tot,im}$  of the calculated APD impedance are shown in Fig. 21(a) and (b). It can be seen that the calculated APD impedance is quite similar to the measured total impedance  $Z$  of the fabricated APD [see Fig. 22(a) and (b)]. For such a LCR-circuit in the avalanche region shown in Fig. 20, an LC resonance is expected and the resonance frequency is estimated by

$$f_{res} = (L_1 C_1)^{-1/2} / (2\pi) = [(v_e + v_h) \alpha' J_0 / \epsilon]^{1/2} / (2\pi), \quad (1)$$

where  $J_0 (= I_0/S)$  is the dc current density.

At low bias voltage, both the inductance  $L_1$  and the series resistance  $R_1$  are large (see Table I), and thus, the resonance

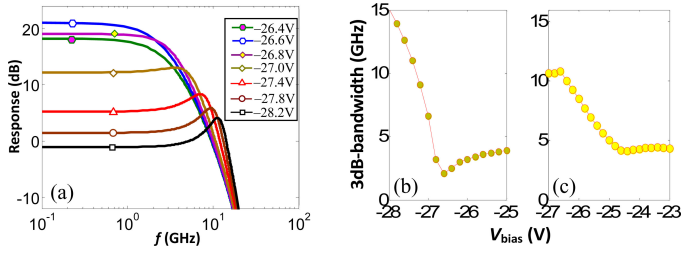


Fig. 23. (a) Calculated frequency responses; (b) Calculated bandwidth; (c) Measured bandwidth. [47].

is weak. In this case, the frequency response is mainly determined by the roll-off due to the  $RC$  constant. Therefore, the peak enhancement cannot be observed in the frequency response. When the bias voltage increases, the series resistance becomes very small (see Table I), and thus, the LC-resonance becomes enhanced. If the series resistance is reduced to zero, one can have the strongest resonance. Meanwhile, since the inductance becomes smaller due to the larger current density at a higher bias voltage, the resonance frequency increases and a peak enhancement can be observed at the high frequency range. This is beneficial to enhance the 3 dB bandwidth as observed in the experimental measurement.

With the equivalent circuit given in Fig. 20, the frequency responses  $R$  can be calculated conveniently, i.e.,  $R = 20 \log(I_L/P_{in})$ , where  $I_L$  is the total ac current (in the unit of ampere) through the load resistance and  $P_{in}$  is the incident optical power (in the unit of watt). From the calculated frequency responses given in Fig. 23(a), one sees that the Ge/Si APD has a frequency response similar to a PIN photodiode when the bias voltage is relatively low. This is because very little impact ionization occurs. When the bias voltage increases, more impact ionization occurs and the dc gain increases [see the responses at low frequency shown in Fig. 23(a)]. Consequently, the build-up time of the avalanche process reduces the bandwidth, as shown in Fig. 23(b) and (c), which show the calculated and measured bandwidths. When the bias voltage increases further (e.g.,  $|V_{bias}| > 26.2V$ ), the response at low frequency decreases due to the space charge effect, while a peak enhancement appears at high frequency [which is observed from the measured responses shown in Fig. 6(a)–(d)] [44]. The calculated and measured 3 dB bandwidths also agree with each other very well, as shown in Fig. 23(b) and (c).

#### D. Temperature Dependence of Ge/Si APDs

APDs are temperature dependent, and it is important to understand how the photodiodes behave when the temperature changes. In Ref. [53], the temperature dependence of normal-incidence Ge/Si SACM APDs with a diameter of  $50 \mu m$  was characterized in the temperature range from 78 to 400 K. Fig. 24(a) shows the measured dark currents at different temperatures. The inset shows the enlarged view for the range around the breakdown voltage. When the temperature decreases, the dark current is depressed significantly as expected and the breakdown voltage  $V_{bd}$  becomes smaller. Fig. 24(b) shows the voltage

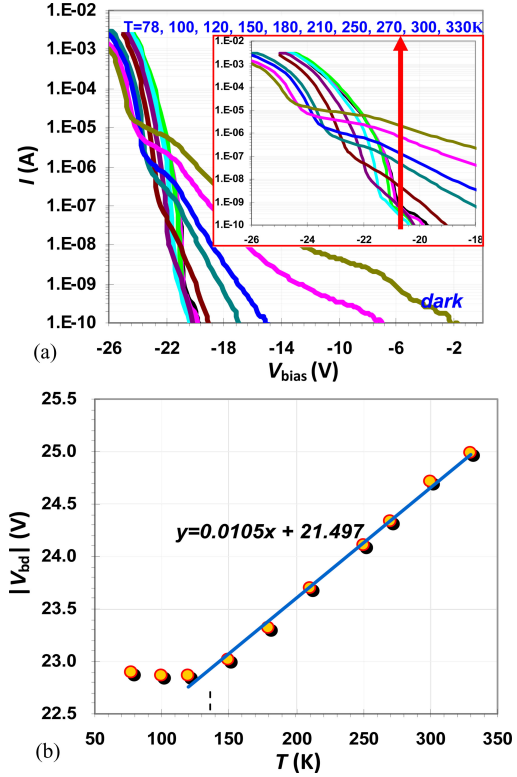


Fig. 24. Measured dark currents of a Ge/Si APD at various temperatures ranging from 78 to 330 K. [53].

$V_{bd}$  as the temperature decreases until the liquid nitrogen temperature (78 K). The breakdown voltage  $V_{bd}$  is defined as the voltage, where the dark current is  $100 \mu A$  [4]. One sees that the voltage  $V_{bd}$  increases as the temperature increases for the Ge/Si APD, which is similar to APDs based on other materials [54]. The reason for such a temperature dependence of the voltage  $V_{bd}$  can be explained as follows [55]. As the temperature increases, the phonon population increases due to the decreased electron–phonon mean path. Thus, higher bias voltage (i.e., higher electric field) is required to overcome the increased carrier cooling caused by phonon scattering, and consequently, to reach breakdown. When using a linear function  $|V_{bd}(T)| = |V_{bd}(T_0)| + \eta(T - T_0)$  to fit the curve  $|V_{bd}| \sim T$ , one has  $\eta = 0.01V/^\circ C$  for the Ge/Si APD. This is six times lower than InP APDs [53].

Since the dark current becomes very low at low temperatures, it will be helpful to measure low-power optical signals. Fig. 25(a) and (b) shows the measured total current and the photo-current as the incident light power decreases from  $-20$  to  $-60$  dBm (1 nW). From these two figures, it can be seen that this Ge/Si APD enables the detection of an optical signal as weak as 1 nW ( $-60$  dBm). Fig. 26 shows the photon current when the input optical power  $P = -20$  dBm as the temperature varies. Due to the temperature dependence of the breakdown voltage, the photo-current increases dramatically at different voltages. At low temperature, a peak photo-current is observed at higher bias voltages, which is due to the space charge effect (similar to those observed at room temperature) [32].

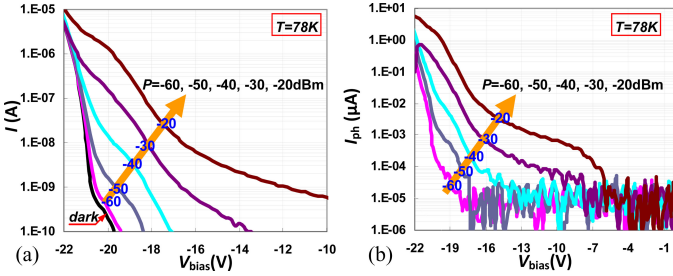


Fig. 25. (a) Measured total currents; (b) Photo-currents. [53].

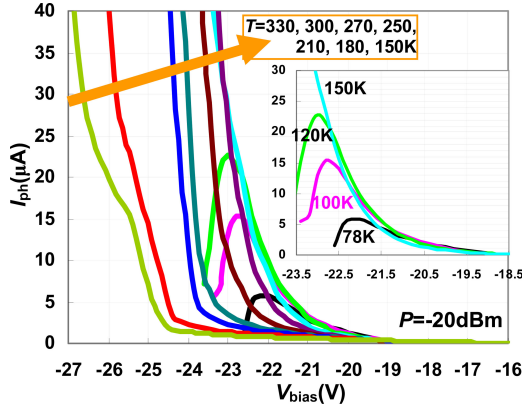


Fig. 26. Temperature dependence of APD photo-currents for a fixed incident light power of  $-20$  dBm.

### III. HIGH POWER Ge/Si UTC PHOTODIODES

#### A. Structure of Ge/Si UTCs

There are numerous design trade-offs between speed, efficiency, and output power. Designing for high bandwidth favors small devices for low capacitance, but designing for high output power favors large devices (with dilute absorption profiles for waveguide structures). In a Si/Ge UTC, the absorption profile and transit-time are controlled primarily by the absorber thickness, while the power-handling and capacitance are controlled primarily by the silicon collector thickness. This *decoupling* allows optimization of the absorption profile independently from the  $RC$ -limited frequency response and compression current and ultimately enables larger bandwidths.

Fig. 27(a) and (b) shows the band diagram and doping profile of a Si/Ge UTC. As with the SACM APD, the electric field in the undoped silicon is much larger than in the germanium absorber. In contrast to the APD, the absorber is fully p-doped and un-depleted under normal operating conditions. A doping grade, rather than the bias voltage, is used to induce an electric field in the absorber such that the electrons move toward the n-side of the diode. Furthermore, no p-type charge layer in the silicon is necessary. Despite these differences, the structures are sufficiently similar that the same model described in Section II-C accurately predicts Si/Ge UTC performance.

High-speed high-power surface-normal [30] and waveguide-type [31] Ge/Si UTC photodiodes have been demonstrated. Layer structures for both devices are shown in Fig. 28(a) and

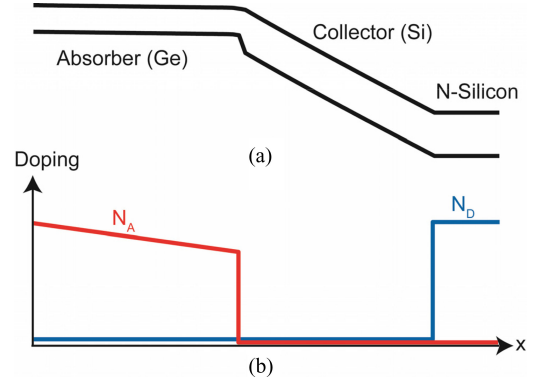


Fig. 27. (a) Band diagram, and (b) doping profile of a Ge/Si UTC photodiode.

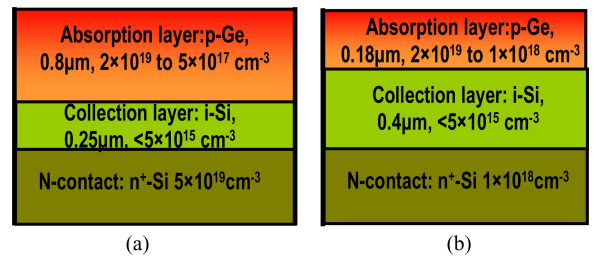


Fig. 28. (a) Layer structure for the surface-normal Si/Ge UTC (b) Layer structure for the waveguide Si/Ge UTC.

(b). The surface-normal device had a bandwidth of 20 GHz, a large-signal 1 dB saturation photocurrent of 20 mA, and a responsivity of 0.3 A/W. The waveguide device was evanescently coupled to improve power handling (relative to a butt-coupled device). It had a bandwidth of 40 GHz and a responsivity in excess of 0.5 A/W, with a slightly lower 1 dB-compression current than the surface-normal device (1.5 mA). Both devices had dark current densities at 1 V bias below 50 mA/cm<sup>2</sup>, which is typical for Si/Ge devices [6].

#### B. Bandwidth of Ge/Si UTCs

The bandwidth of a surface-normal 14  $\mu\text{m}$  diameter device is shown in Fig. 29(a). The 3 dB bandwidth at 2 V and larger biases is 20 GHz. The bandwidth is limited by both the  $RC$  charging time and the transit time. Fig. 29(a) also shows two theoretical curves. The theoretical curves have two parts: a transit-time and an  $RC$  contribution. For the transit-time contribution, we used the expression for the short-circuit current  $I_{sc}$  in [46], neglecting the effect of impact ionization. In this case, the expression in [46] simplifies to the expression found in [57]. We found that in order to accurately fit the data, we needed to modify the boundary condition at the p-contact to account for backwards diffusion of electrons. The two theoretical curves shown in the plot correspond to transit time contribution calculated using [46] and [57] directly and to the modified equation. For the  $RC$  charging time, we fit the microwave reflection ( $S_{22}$ ) data to find the impedance  $Z$ , series resistance  $R_s$ , and probe parasitic parameters. This fit is shown in Fig. 29(b). The measured impedance is then used

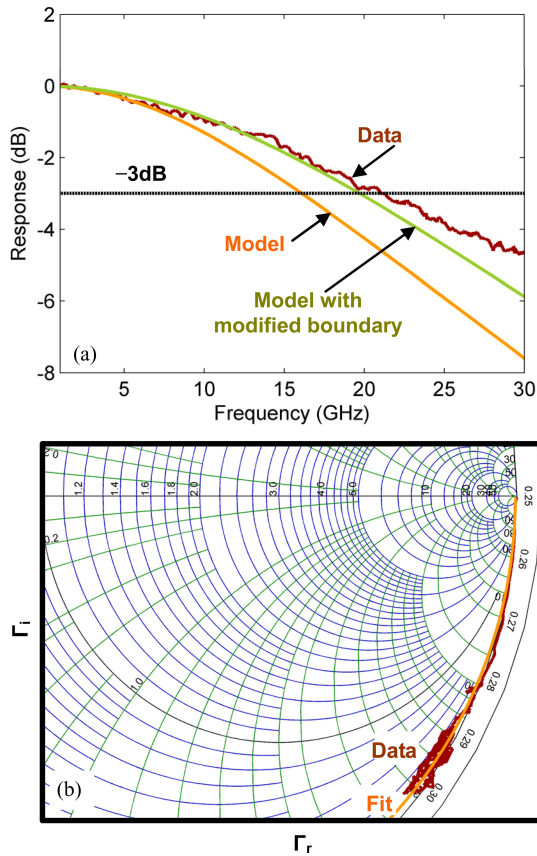


Fig. 29. (a) Measured and calculated frequency response of a surface-normal Si/Ge UTC. The measured response is shown in red. The theoretical response calculated using [46] reflection data are shown in orange, and the theoretical response using a slightly modified version of the expression in [46] is shown in green. (b) Measured (red) and fit (orange) microwave reflection coefficient from 0 to 20 GHz.

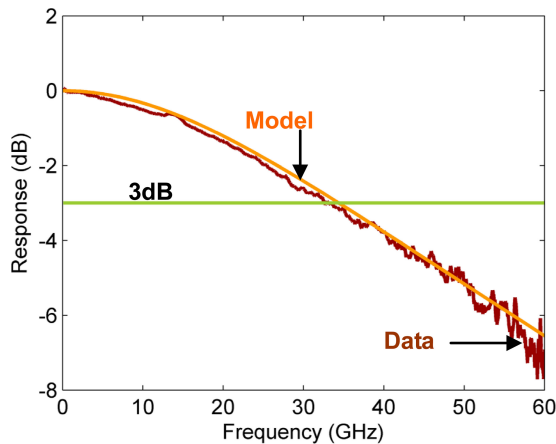


Fig. 30. Frequency response of a waveguide PD.

in conjunction with the equation  $I_L = I_{sc} \kappa$  to generate the theoretical curves shown on the graph.

Fig. 30 shows the frequency response of a  $3 \mu\text{m} \times 90 \mu\text{m}$  waveguide photodiode at  $-5 \text{ V}$  bias. The 3 dB electrical bandwidth is 33 GHz, and 40 GHz Si/Ge UTCs with the same cross-

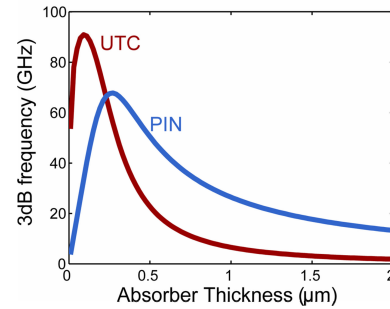


Fig. 31. Maximum attainable bandwidths for  $4 \mu\text{m} \times 15 \mu\text{m}$  Si/Ge UTCs and PINs with the same germanium thicknesses and dimensions.

sectional design have been demonstrated as well [31]. The theoretical frequency response of the  $3 \mu\text{m} \times 90 \mu\text{m}$  detector was calculated using the method described earlier and is also shown. As with the surface-normal detectors, the theoretical curve fits well with the data.

As our experimental results indicate, the expression for the frequency response of an SACM APD derived in [46] can be used to accurately model the bandwidth of a UTC photodiode. It is then interesting to compare the performance of the UTC to the performance of comparable PIN photodiodes. Fig. 31 shows the simulated bandwidth of a  $4 \mu\text{m} \times 15 \mu\text{m}$  photodiode as a function of germanium thickness for both PIN and UTC structures. Parasitic effects (e.g., pad capacitance and contact resistance) were ignored in the simulation, and the diode impedance  $Z$  was taken from the analytical expressions in [46]. The collector thickness for the UTC was chosen to optimize bandwidth. As the figure shows, for thick absorbers, a PIN structure is preferable. This is because these structures are transit-time limited, and adding a depleted silicon layer only serves to increase the transit time. For thin absorbers, such as the 175 nm thick absorber used in [31], the UTC structure yields higher bandwidth. This is because the silicon collector can be adjusted to decrease the capacitance. Furthermore, the structure with the highest bandwidth is a UTC rather than a PIN. This indicates that for applications requiring very high bandwidth, a UTC rather than a PIN should be used. For devices with larger dimensions than the  $60 \mu\text{m}^2$  device considered here, the qualitative conclusions are the same, but the absorber thickness at which a UTC becomes preferable to a PIN is larger.

### C. Output Power of Ge/Si UTCs

For both avalanche photodetectors and photodiodes operating in the large-signal regime, it is important to include the effect of the external circuit in order for a model to be accurate. For avalanche photodetectors, this is necessary in order to capture the time delay between the ac current and terminal voltage (due to the avalanche build-up effect) that causes the inductive peaking, as discussed earlier. For high-power photodiodes, it is necessary because the saturation current, or the current at which the photodiode output will appear clipped, depends on the terminal voltage [58]. Under large-signal operation, the position-dependence of the electric field becomes important [58], and

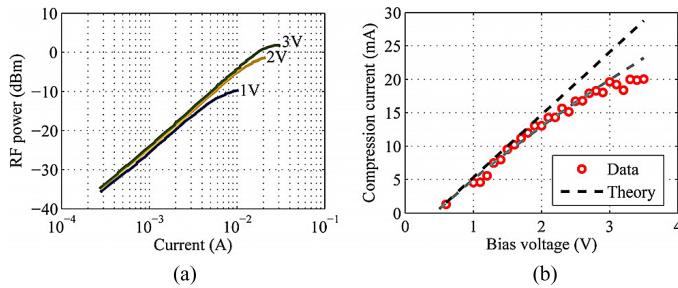


Fig. 32. (a) Output RF power at 20 GHz as a function of photocurrent. (b) 1 dB compression current as a function of bias voltage. Circles: Measured data; upper line: 1 dB compression current predicted by model without thermal effects; lower line: model with thermal effects [30].

an accurate model must include this as well. The matrix-based model developed in [47] incorporates both of these effects and can be applied to Si/Ge UTCs to predict their power-handling performance.

Fig. 32(a) and (b) shows the measured and simulated power-handling characteristics of the surface-normal Si/Ge UTC. An 80% modulation depth tone fixed at 20 GHz was generated using the standard heterodyne technique with two free-running lasers at 1537 nm, and the output power was measured on an RF spectrum analyzer. Both data and theory are shown in Fig. 32(b). Because the device was backside-illuminated, the photocurrent was approximately uniform, and the 1-D model developed in [47] accurately describes device performance. For waveguide photodiodes, where the current distribution is highly non-uniform [56], finite-element methods can be used in conjunction with the 1-D model [59].

It should be noted that if it is assumed that the electron velocity in the collector is either zero or its saturated value, then the position-dependent value of the electric field in the collector can be found analytically, and the matrix method is not necessary [60]. This was the approach used to generate the theoretical curves shown in the figure. Using the matrix method in conjunction with a continuous velocity-field relation instead is expected to yield more accurate results.

#### IV. CONCLUSION

In this paper, we have given a review for the resonant APDs and UTC-PDs operating at 1310~1550 nm with the Ge/Si material system. This material system has proven convenient for realizing high-performance monolithic photodetectors by utilizing some specific decoupled structures, including resonant APDs and UTC photodiodes.

In particular, high-speed and high gain resonant APDs can be realized by using an SACM structure with a Ge absorption region as well as a Si avalanche region (for multiplication), which decouples the carrier generation and the avalanche ionization spatially so that the Ge and Si layers can be optimized separately to achieve excellent performances (high quantum efficiency, GBP and sensitivity). According to the small signal models and the derived equivalent circuits for such a Ge/Si SACM APD, it has been shown that there is an *LC* resonance

when the APD is operating at a high bias, which is the origin of the peak enhancement in the frequency response of the resonant Ge/Si SACM APDs. By utilizing this kind of peak enhancement, a large 3 dB-bandwidth can be achieved for an APD, which is helpful to obtain an extremely high gain-bandwidth. The importance of an *LC* resonance has been realized for the bandwidth enhancement of PDs, and it is even possible to introduce an external inductor to increase the bandwidth of PDs [61], [62]. Therefore, the derived new equivalent circuit of Ge/Si SACM APDs will be helpful when one tries to introduce an optimal external inductor to increase the bandwidth, and thus, the GBP. The Ge/Si UTC photodiode, which includes a Ge absorption region and an intrinsic silicon layer to decouple the light absorption from carrier collection, has also been realized. The high bandwidth, high saturation current, and low thermal impedance of the device is promising for use in high-power applications.

In a summary, the Ge/Si material system has many intrinsic advantages, such as CMOS compatibility, high light-absorption of Ge, low *k*-value of silicon, and high thermal conductivities of Si and Ge. This makes Ge/Si a very promising platform to realize monolithic photodetectors as the key components for various applications of silicon photonics. Furthermore, the silicon substrate makes it possible to have electronic circuits integrated together with photodetectors. For example, it is promising to develop high-speed receivers by integrating Ge/Si (A)PDs with other elements (like wavelength-division-multiplexing devices) monolithically. A Ge/Si (A)PD array even enables multi-channel receivers as well as on-chip micro-spectrometers. On the other hand, the dark current density in Ge photodiodes is still around two orders higher than III-V photodetectors due to thermionic emission limits and dislocation densities. It is desired to improve the Ge-growth process as well as the Ge/Si (A)PD design to lower the dark current so that it is attractive to expand the application of Ge/Si APDs to more fields, such as single-photon detection.

#### ACKNOWLEDGMENT

The authors would like to thank Y. Kang, M. Morse, J. C. Campbell, and A. Pauchard for useful discussions. The authors thank Intel for supplying the APD devices measured here.

#### REFERENCES

- [1] C. Batten, A. Joshi, J. Orcutt, A. Khilo, B. Moss, C. W. Holzwarth, M. A. Popovic, H. Q. Li, H. I. Smith, J. L. Hoyt, F. X. Kartner, R. J. Ram, V. Stojanovic, and K. Asanovic, "Building many-core processor-to-DRAM networks with monolithic CMOS silicon photonics," *IEEE Micro.*, vol. 29, no. 4, pp. 8–21, Aug. 2009.
- [2] A. W. Fang, H. Park, O. Cohen, R. Jones, M. J. Paniccia, and J. E. Bowers, "Electrically pumped hybrid AlGaInAs-silicon evanescent laser," *Opt. Exp.*, vol. 14, pp. 9203–9210, 2006.
- [3] A. Y. Liu, C. Zhang, J. Norman, A. Snyder, D. Lubyshyev, J. M. Fastenau, A. W. K. Liu, A. C. Gossard, and J. E. Bowers, "High performance continuous wave 1.3  $\mu\text{m}$  quantum dot lasers on silicon," *Appl. Phys. Lett.*, vol. 104, p. 041104, 2014.
- [4] Y. Kang, H.-D. Liu, M. Morse, M. J. Paniccia, M. Zadka, S. Litski, G. Sarid, A. Pauchard, Y.-H. Kuo, H.-W. Chen, W. S. Zaoui, J. E. Bowers, A. Beling, D. C. McIntosh, X. Zheng, and J. C. Campbell, "Monolithic Ge/Si avalanche photodiodes with 340 GHz gain-bandwidth product," *Nature Photon.*, vol. 3, no. 1, pp. 59–63, 2009.

- [5] N. Duan, T.-Y. Liow, A. E.-J. Lim, L. Ding, and G. Q. Lo, "310 GHz gain-bandwidth product Ge/Si avalanche photodetector for 1550 nm light detection," *Opt. Exp.*, vol. 20, pp. 11031–11036, 2012.
- [6] J. Michel, J. F. Liu, and L. C. Kimerling, "High performance Ge-on-Si photodetectors," *Nature Photon.*, vol. 4, no. 8, pp. 527–534, 2010.
- [7] A. R. Hawkins, W. Wu, P. Abraham, K. Streubel, and J. E. Bowers, "High gain-bandwidth-product silicon heterointerface photodetector," *Appl. Phys. Lett.*, vol. 70, no. 3, pp. 303–305, 1996.
- [8] M. Rouvière, M. Halbwx, J.-L. Cercus, E. Cassan, L. Vivien, D. Pascal, M. Heitzmann, J.-M. Hartmann, and S. Laval, "Integration of germanium waveguide photodetectors for intrachip optical interconnects," *Opt. Eng.*, vol. 44, pp. 75402–75406, 2005.
- [9] L. Vivien, M. Rouvière, J.-M. Fédéli, D. Marris-Morini, J. F. Damlencourt, J. Mangeney, P. Crozat, L. El Melhaoui, E. Cassan, X. L. Roux, D. Pascal, and S. Laval, "High speed and high responsivity germanium photodetector integrated in a silicon-on-insulator microwaveguide," *Opt. Exp.*, vol. 15, pp. 9843–9848, 2007.
- [10] Y. Ishikawa, K. Wada, D. D. Cannan, J. Liu, D. L. Hsin-Chiao, and L. C. Kimerling, "Strain-induced band gap shrinkage in Ge grown on Si substrate," *Appl. Phys. Lett.*, vol. 82, pp. 2044–2046, 2002.
- [11] S. Fama, L. Colace, G. Masini, G. Assanto, H.-C. Luan, "High performance germanium-on-silicon detectors for optical communications," *Appl. Phys. Lett.*, vol. 81, pp. 586–588, 2002.
- [12] M. Halbwx, M. Rouvière, Y. Zheng, D. Debarre, L. H. Nguyen, J.-L. Cercus, C. Clerc, V. Yam, S. Laval, E. Cassan, and D. Bouchier, "UHV-CVD growth and annealing of thin fully relaxed Ge films on (0 0 1)Si," *Opt. Mater.*, vol. 27, pp. 822–826, 2005.
- [13] J.-M. Hartmann, A. Abbadié, A. M. Papon, P. Holliger, G. Rolland, T. Billon, J.-M. Fédéli, M. Rouvière, L. Vivien, and S. Laval, "Reduced pressure–chemical vapor deposition of Ge thick layers on Si(001) for 1.3–1.55- $\mu\text{m}$  photodetection," *J. Appl. Phys.*, vol. 95, pp. 5905–5907, 2004.
- [14] L. Colace, G. Masini, F. Galluzzi, G. Assanto, G. Capellini, L. Di Gaspare, E. Palange, and F. Evangelisti, "Metal semiconductor-metal near-infrared light detector based on epitaxial Ge/Si," *Appl. Phys. Lett.*, vol. 72, no. 24, pp. 3175–3177, Jun. 1998.
- [15] H.-C. Luan *et al.*, "High-quality Ge epilayers on Si with low threading-dislocation densities," *Appl. Phys. Lett.*, vol. 75, pp. 2909–2911, 1999.
- [16] M. Halbwx *et al.*, "Kinetics of Ge growth at low temperature on Si (001) by ultrahigh vacuum chemical vapor deposition," *J. Appl. Phys.*, vol. 97, p. 064907, 2005.
- [17] L. Chen, P. Dong, and M. Lipson, "High performance germanium photodetectors integrated on submicron silicon waveguides by low temperature wafer bonding," *Opt. Exp.*, vol. 16, pp. 11513–11518, 2008.
- [18] J. Liu, R. Camacho-Aguilera, J. T. Bessette, X. Sun, X. Wang, Y. Cai, L. C. Kimerling, and J. Michel, "Ge-on-Si optoelectronics," *Thin Solid Films*, vol. 520, pp. 3354–3360, 2012.
- [19] J. E. Bowers and C. A. Burrus, "Ultra-wide band long-wavelength PIN photodetectors," *J. Lightw. Technol.*, vol. LT-5, no. 10, pp. 1339–1350, Oct. 1987.
- [20] J. E. Bowers and C. A. Burrus, "High speed zero bias waveguide photodetectors," *Electron. Lett.*, vol. 22, no. 17, pp. 905–906, Aug. 1986.
- [21] S. J. Koester, J. D. Schaub, G. Dehlinger, and J. O. Chu, "Germanium-on-SOI infrared detectors for integrated photonic applications," *IEEE J. Sel. Topics Quantum Electron.*, vol. 12, no. 6, pp. 1489–1502, Nov./Dec. 2006.
- [22] D. Ahn, C.-Y. Hong, J. Liu, W. Giziewicz, M. Beals, L. C. Kimerling, J. Michel, J. Chen, and F. X. Kärtner, "High performance, waveguide integrated Ge photodetectors," *Opt. Exp.*, vol. 15, pp. 3916–3921, 2007.
- [23] A. R. Hawkins, W. Wu, P. Abraham, K. Streubel, and J. E. Bowers, "High gain-bandwidth-product silicon heterointerface photodetector," *Appl. Phys. Lett.*, vol. 70, no. 3, pp. 303–305, Jan. 1997.
- [24] J. C. Campbell, S. Demiguel, F. Ma, A. Beck, X. Guo, S. Wang, X. Zheng, X. Li, J. D. Beck, M. A. Kinch, A. Huntington, L. A. Coldren, J. Decobert, and N. Tschertner, "Recent advances in avalanche photodiodes," *IEEE J. Sel. Topics Quantum Electron.*, vol. 10, no. 4, pp. 777–787, Jul./Aug. 2004.
- [25] Z. Lu, Y. Kang, C. Hu, Q. Zhou, H.-D. Liu, and J. C. Campbell, "Geiger-mode operation of Ge-on-Si avalanche photodiodes," *IEEE J. Quantum Electron.*, vol. 47, no. 5, pp. 731–735, May 2011.
- [26] D. Guckenberger, "Microwave photonic applications for silicon photonics," presented at the Optical Fiber Communication Conf., San Diego, CA, USA, 2009, Paper OWS1.
- [27] L. Vivien, A. Polzer, D. Marris-Morini, J. Osmond, J. M. Hartmann, P. Crozat, E. Cassan, C. Kopp, H. Zimmermann, and J. M. Fédéli, "Zero-bias 40 Gbit/s germanium waveguide photodetector on silicon," *Opt. Exp.*, vol. 20, no. 2, pp. 1096–1101, Jan. 2012.
- [28] H.-Y. Xue, C.-L. Xue, B.-W. Cheng, Y.-D. Yu, and Q.-M. Wang, "High-saturation-power and high-speed Ge-on-SOI p-i-n photodetectors," *IEEE Electron Device Lett.*, vol. 31, no. 7, pp. 701–703, Jul. 2010.
- [29] A. Ramaswamy, M. Piels, N. Nunoya, T. Yin, and J. E. Bowers, "High power silicon-germanium photodiodes for microwave photonic applications," *IEEE Trans. Microw. Theory Technol.*, vol. 58, no. 11, pp. 3336–3343, Nov. 2010.
- [30] M. Piels and J. E. Bowers, "Ge/Si uni-traveling carrier photodetector," *Opt. Exp.*, vol. 20, pp. 7488–7495, 2012.
- [31] M. Piels and J. E. Bowers, "40 GHz Si/Ge uni-traveling carrier photodiode," *J. Lightw. Technol.*, to be published.
- [32] W. S. Zaoui, H.-W. Chen, J. E. Bowers, Y. Kang, M. Morse, M. J. Paniccia, A. Pauchard, and J. C. Campbell, "Frequency response and bandwidth enhancement in Ge/Si avalanche photodiodes with over 840 GHz gain-bandwidth-product," *Opt. Exp.*, vol. 17, pp. 12641–12649, 2009.
- [33] C. T. DeRose, D. C. Trotter, W. A. Zortman, A. L. Starbuck, M. Fisher, M. R. Watts, and P. S. Davids, "Ultra compact 45 GHz CMOS compatible germanium waveguide photodiode with low dark current," *Opt. Exp.*, vol. 19, pp. 24897–24904, 2011.
- [34] J. F. Liu, J. Michel, W. Giziewicz, D. Pan, K. Wada, D. Cannon, L. C. Kimerling, J. Chen, F. O. Ilday, F. X. Kärtner, and J. Yasaitis, "High-performance, tensile strained Ge p-i-n photodetectors on a Si platform," *Appl. Phys. Lett.*, vol. 87, p. 103501, 2005.
- [35] M. Jutzi, M. Berroth, G. Wohl, M. Oehme, E. Kasper, "Ge-on-Si vertical incidence photodiodes with 39-GHz bandwidth," *IEEE Photon. Technol. Lett.*, vol. 17, no. 7, pp. 1510–1512, Jul. 2005.
- [36] M. Morse, O. Dosunmu, G. Sarid, and Y. Chetrit, "Performance of Ge-on-Si p-i-n photodetectors for standard receiver modules," *IEEE Photon. Technol. Lett.*, vol. 18, no. 23, pp. 2442–2444, Dec. 2006.
- [37] S. Klinger, M. Berroth, M. Kaschel, M. Oehme, and E. Kasper, "Ge-on-Si p-i-n photodiodes with a 3 dB bandwidth of 49 GHz," *IEEE Photon. Technol. Lett.*, vol. 21, no. 13, pp. 920–922, Jul. 2009.
- [38] D. Dai, H.-W. Chen, J. E. Bowers, Y. Kang, M. Morse, and M. J. Paniccia, "Equivalent circuit model of a waveguide-type Ge/Si avalanche photodetector," *Physica Status Solidi (c)*, vol. 7, no. 10, pp. 2532–2535, Oct. 2010.
- [39] L. Virost, L. Vivien, J.-M. Fédéli, Y. Bogumilowicz, J.-M. Hartmann, F. Bœuf, P. Crozat, D. Marris-Morini, and E. Cassan, "High-performance waveguide-integrated germanium PIN photodiodes for optical communication applications," *Photon. Res.*, vol. 1, pp. 140–147, 2013.
- [40] Y. Kang, Z. Huang, Y. Saado, J. Campbell, A. Pauchard, J. Bowers, and M. Paniccia, "High performance Ge/Si avalanche photodiodes development in intel," presented at the Optical Fiber Communication Conf./Nat. Fiber Optic Engineers Conf., Los Angeles, CA, USA, 2011, Paper OWZ1.
- [41] H. S. Kang, M. J. Lee, and W. Y. Choi, "Si avalanche photodetectors fabricated in standard complementary metal-oxide-semiconductor process," *Appl. Phys. Lett.*, vol. 90, pp. 151118–1–151118-3, 2007.
- [42] J. W. Shi, Y. S. Wu, Z. R. Li, and P. S. Chen, "Impact-ionization-induced bandwidth-enhancement of a Si-SiGe-based avalanche photodiode operating at a wavelength of 830 nm with a gain-bandwidth product of 428 GHz," *IEEE Photon. Technol. Lett.*, vol. 19, no. 7, pp. 474–476, Apr. 2007.
- [43] M.-J. Lee, H.-S. Kang, and W.-Y. Choi, "Equivalent circuit model for Si avalanche photodetectors fabricated in standard CMOS process," *IEEE Electron Device Lett.*, vol. 29, no. 10, pp. 1115–1117, Oct. 2008.
- [44] D. Dai, H.-W. Chen, J. E. Bowers, Y. Kang, M. Morse, and M. J. Paniccia, "Resonant normal-incidence separate-absorption-charge-multiplication Ge/Si avalanche photodiodes," *Opt. Exp.*, vol. 17, no. 19, pp. 16549–16557, 2009.
- [45] G. Kim, I. G. Kim, J. H. Baek, and O. K. Kwon, "Enhanced frequency response associated with negative photoconductance in an InGaAs/InAlAs avalanche photodetector," *Appl. Phys. Lett.*, vol. 83, no. 6, pp. 1249–1251, 2003.
- [46] D. Dai, M. Rodwell, J. E. Bowers, Y. Kang, and M. Morse, "Derivation of the small signal response and equivalent circuit model for a separate absorption and multiplication layer avalanche photodetector," *IEEE J. Sel. Topics Quantum Electron.*, vol. 16, no. 5, pp. 1328–1336, Sep./Oct. 2010.
- [47] D. Dai and J. E. Bowers, "Simple matrix-method modeling for avalanche photodetectors with arbitrary layer structures and absorption/multiplication coefficients," *J. Lightw. Technol.*, vol. 28, no. 10, pp. 1404–1413, May 2010.

- [48] S. M. Sze, *Physics of Semiconductor Devices*. New York, NY, USA: Wiley, 1981, ch. 5.
- [49] W. Sun, Y. Fu, Z. Lu, and J. Campbell, "Study of bandwidth enhancement and non-linear behavior in avalanche photodiodes under high power condition," *J. Appl. Phys.*, vol. 113, p. 044509, 2013.
- [50] T. Misawa, "Multiple uniform layer approximation in analysis of negative resistance in p-n junction in breakdown," *IEEE Trans. Electron Device*, vol. ED-14, no. 12, pp. 795–808, Dec. 1967.
- [51] F. K. Manasse and J. S. Shapiro, "An improved dispersion relationship for the P-N junction avalanche diode," *IEEE Trans. Electron Devices*, vol. ED-15, no. 5, pp. 282–289, May 1968.
- [52] Y.-C. Wang, "Small-signal characteristics of a read diode under conditions of field-dependent velocity and finite reverse saturation current," *Solid State Electron.*, vol. 21, no. 4, pp. 609–615, 1978.
- [53] D. Dai, J. E. Bowers, and Y. Kang, "The characterization of normal incidence Ge/Si avalanche photodiodes (APDs) at low temperatures," in *Proc. IEEE Winter Top.*, 2011, pp. 121–122.
- [54] Y. G. Xiao, "Temperature dependent studies of InP/InGaAs avalanche photodiodes based on time domain modeling," *IEEE Trans. Electron Devices*, vol. 48, no. 4, pp. 661–670, Apr. 2001.
- [55] M. Azadeh, *Fiber Optics Engineering*, New York, NY, USA: Springer, 2009, ch. 6.
- [56] K. S. Giboney, M. J. W. Rodwell, and J. E. Bowers, "Traveling wave photodetector design and measurements," *IEEE J. Sel. Topics Quantum Electron.*, vol. 2, no. 9, pp. 622–629, Sep. 1996.
- [57] T. Ishibashi, S. Kodama, N. Shimizu, and T. Furuta, "High-speed response of uni-traveling-carrier photodiodes," *Jpn. J. Appl. Phys.*, vol. 36, pp. 6263–6268, 1997.
- [58] K. J. Williams and R. D. Esman, "Design considerations for high-current photodetectors," *J. Lightw. Technol.*, vol. 17, no. 8, pp. 1443–1454, Aug. 1999.
- [59] M. Piels, A. Ramaswamy, and J. Bowers, "Nonlinear modeling of waveguide photodetectors," *Opt. Exp.*, vol. 21, pp. 15634–15644, 2013.
- [60] C. T. Kirk, "A theory of transistor cutoff frequency (f<sub>T</sub>) falloff at high current densities," *IEEE Trans. Electron Devices*, vol. ED-9, no. 2, pp. 164–174, 1962.
- [61] M. Gould, T. Baehr-Jones, R. Ding, and M. Hochberg, "Bandwidth enhancement of waveguide-coupled photodetectors with inductive gain peaking," *Opt. Exp.*, vol. 20, pp. 7101–7111, 2012.
- [62] A. Novack, M. Gould, Y. Yang, Z. Xuan, M. Streshinsky, Y. Liu, G. Capellini, A. Eu-Jin Lim, G.-Q. Lo, T. Baehr-Jones, and M. Hochberg, "Germanium photodetector with 60 GHz bandwidth using inductive gain peaking," *Opt. Exp.*, vol. 21, pp. 28387–28393, 2013.



**Molly Piels** received the B.S. degree in engineering and the B. A. degree in history from Swarthmore College, Swarthmore, PA, USA, in 2008 and the M.S. and Ph.D. degrees in electrical and computer engineering from the University of California, Santa Barbara, CA, USA, in 2009 and 2013, respectively. She is currently a Postdoc in the Metro-Access and Short Range Systems group, DTU Fotonik, Lyngby, Denmark, where her research interests include coherent communication and space division multiplexing.



**John E. Bowers** (F'93) received the M.S. and Ph.D. degrees from Stanford University, Stanford, CA, USA. He is Director of the Energy Efficiency Institute and a Professor in the Department of Electrical and Computer Engineering, University of California, Santa Barbara (UCSB), CA, USA. He is also a cofounder of Terabit Technology, Calient Networks, and Aurion. His research interests are primarily concerned with silicon photonics, optoelectronic devices, optical switching, and transparent optical networks.

He worked for AT&T Bell Laboratories and Honeywell before joining the UCSB. He has published eight book chapters, 600 journal papers, 800 conference papers and has received 52 patents. He is a Fellow of the IEEE, OSA and the American Physical Society, and received of the OSA/IEEE Tyndall Award, the OSA Holonyak Award, the IEEE LEOS William Streifer Award and the South Coast Business and Technology Entrepreneur of the Year Award. He is a member of the National Academy of Engineering. He and his coworkers received the ACE Award for Most Promising Technology for the hybrid silicon laser in 2007.



**Daoxin Dai** (M'07) received the B. Eng. degree from the Department of Optical Engineering, Zhejiang University, Hangzhou, China, and the Ph.D. degree from the Royal Institute of Technology, Stockholm, Sweden, in 2000 and 2005, respectively. He joined Zhejiang University as an Assistant Professor in 2005 and became an Associate Professor in 2007 and a Full Professor in 2011. He visited the Chinese University of Hong Kong in 2005, and Inha University (Korea) in 2007. He worked at the University of California, Santa Barbara, CA, USA, as a Visiting

Scholar from the end of 2008 until 2011. His current research interests include silicon nanophotonics for optical interconnections and optical sensing. He has published about 110 refereed international journals papers, and holds 9 patents. He has been invited to give more than ten invited talks and served as the program committee member or session chair for some top international conferences. He is serving as the Associate Editor of the *Journals of Optical and Quantum Electronics and Photonics Research*.